

Superficial simplicity of the 2010 M_w 7.2 El Mayor-Cucapah earthquake of Baja California, Mexico

Shengji Wei¹, Eric Fielding², Sebastien Leprince¹, Anthony Sladen¹, Jean-Philippe Avouac¹, Don Helmberger¹, Egill Hauksson¹, Risheng Chu¹, Mark Simons¹, Kenneth Hudnut^{1,3}, Thomas Herring⁴ and Richard Briggs⁵

1, Division of Geological and Planetary Sciences, California Institute of Technology, Pasadena, CA 91125, USA

2, Jet Propulsion Laboratory, California Institute of Technology, Pasadena, CA 91109, USA

3, United States Geological Survey, Pasadena, CA 91106, USA

4, Department of Earth, Atmospheric, and Planetary Sciences, Massachusetts Institute of Technology, Cambridge, MA 02139, USA

5, United States Geological Survey, Golden, CO 80225, USA

The M_w 7.2 2010 El Mayor-Cucapah earthquake that ruptured an apparently relatively straight fault trace had a moment tensor that differed significantly from predictions based on a single planar elastic shear-dislocation. The 120 km long rupture extended from the US Mexico international boarder, along a fault system in the Sierra Cucapah to the Gulf of California in the southeast. At depth, the rupture involved two N130°E striking segments with opposite dip angles connected by a jog with a N15°W striking normal segment. The earthquake initiated as a moderate normal event at this jog before rupturing bilaterally the two main segments with dominantly strike-slip motion. The complexity of the subsurface fault geometry and the distribution of slip orientation that is constrained by seismological, remote sensing, and geodetic data account for the large non-double-couple component of the moment tensor.

The El Mayor-Cucapah Earthquake (EMC) that occurred on April 4, 2010 produced extensive liquefaction in the Colorado River delta area and in the Mexicali and Imperial Valleys, and numerous rockfalls occurred in the Sierra Cucapah. This is the largest earthquake to have struck the southern California and northern Baja California, Mexico area since the $M_w 7.3$, Landers Earthquake of 1992¹. The GCMT (global centroid moment tensor) of the mainshock reveals a double couple component corresponding to scalar moment of $7.28 \times 10^{19} \text{N}\cdot\text{m}$ ($M_w 7.17$), with a significant non-double-couple (CLVD) component ($2.4 \times 10^{19} \text{N}\cdot\text{m}$) (Fig. 1)². The mainshock occurred where the system of continental parallel right-lateral strike-slip faults including the San Andreas, San Jacinto and Elsinore faults, connect with a system of transform faults and active spreading centers in the Gulf of California to the south³ (Fig. 1 and fig. S1). This fault system forms the plate boundary in southern California, where the Pacific plate moves northwestwards with respect to North America at about 46 mm/yr (Fig.1 inset). The main active fault recognized in the area was the Laguna Salada fault (LSF), a right-lateral normal oblique fault bounding the Sierra Cucapah to the west. It accommodated a $M_w 7.1$ earthquake in 1892⁴(fig. S1).

We synthesize the earthquake data using modern methods in seismology, tectonic geodesy, remote-sensing (Global Positioning Systems (GPS), Interferometric Synthetic Aperture Radar (InSAR), sub-pixel correlation of optical satellite images and Synthetic Aperture Radar (SAR)). The remote-sensing data reveal an almost linear and continuous fault trace extending over about 120 km from the northern tip of the Sierra Cucapah to the Gulf of California, with a right-lateral slip of about 2m on average (Fig.1). These data indicate that the April 4 mainshock didn't rupture the LSF but rather two other faults, the Borrego and Pescadores faults within the Sierra Cucapah, which had been mapped but not recognized to be active⁴ (fig. S1). Our data also reveal

a major strike-slip segment which extends from the epicenter to the southeast, across the Colorado River Delta. This part of the mainshock rupture that had been verified in the field and named the Indiviso fault⁵ occurred along basement faults beneath the sedimentary deposits of the Colorado River. So, the surface trace does not coincide with previously-identified active faults with an obvious geomorphic expression, such as the Laguna Salada Fault or the Canada David Detachment. Rather, the earthquake ruptured along a complex set of existing faults, illustrating the ongoing process by which the slip along Elsinore fault connects to the transform plate boundary in the Gulf of California.

Overall, the location and focal-mechanism of the earthquake are consistent with right-lateral slip along the right-lateral transform plate boundary fault system (Fig. 1). However, the large non-double couple component of the moment tensor suggests a substantial component of normal faulting. The modeling of the first 15s of the teleseismic waveforms (fig. S2) requires that the earthquake initiated as a normal event near the epicenter (Fig.1). This observation, together with the clear asymmetry of surface strain seen from the correlation of the optical (SPOT) and SAR images (Japanese Aerospace Exploration Agency ALOS PALSAR) as well as from InSAR analysis of PALSAR and European Space Agency Envisat ASAR (See Supplements), require a complex fault geometry at depth which seems at odds with the relatively straight strike-slip fault trace observed at the surface (Fig 2).

We use finite-fault source modeling to determine what geometry and slip-distribution reconcile all the observations gathered in this study. We discretized the rupture zone into slipping patches (point sources) which contribute to the wave-field at a particular time controlled by the rupture velocity and rise-time⁶. Trade-offs among the amplitude of slip, the rupture velocity, and the rise-time^{7,8} are limited because constraints on the fault geometry are provided

by the remote-sensing observations. We concentrate on geometrical fault irregularities that can influence large events⁹ but are not easily resolved by seismology alone. We built the simplest possible fault geometry required to fit our observations. We chose a N355°E striking fault plane dipping 45° to the east (F1) to account for the teleseismic waveforms (fig. S2) and to match the local alignment of aftershocks near the epicenter. Segments F2 (51km long, striking N312°E), F3 (60km long, striking N132°E) and F4 (18km long, striking N335°E) were defined to follow the surface trace. We use the geodetic and InSAR data to determine the best fitting dip angles based on a 5° grid-search steps. The best dip angles are 75° to the west for F2 and 60° to the east for F3 and 50° to the east for F4. The GPS data (presented as vectors in Fig. 1) are recorded by stations located in the U.S. These are closest to the northern segment, and constrain the dip angle of F4. The dip angles of F2 and F3 are mostly controlled by the InSAR data (see Supplements for details). Although the fault must be more complex at a finer scale, we are able to explain the bulk of our combined datasets with these four segments.

To generate the kinematic model, we invert for the distribution of slip in terms of rake direction, amplitude of slip, rupture velocity and rise time¹⁰. Using the geodetic data (GPS and remote-sensing) we first determine a static co-seismic slip model representing the cumulative slip distribution due to the earthquake (fig. S3). We use the horizontal offsets measured from the SAR and SPOT images to constrain the fault slip at the surface (Fig. 2a), and the whole geodetic and InSAR dataset to constrain the static displacement field. Because of the simplified fault geometry, the formal inversion of shallow slip would indeed be biased to lower slip wherever the fault model does not follow exactly the measured fault trace. To avoid this bias, we impose slip on the shallow portion of the fault to fit the horizontal surface slip measured from the SAR and SPOT to within the average 2- σ uncertainty on these measurements ($\pm 0.5\text{m}$) (Fig. 3a)¹¹. To

restrict the large number of data points to be inverted, we resample the unwrapped interferograms¹² (figs. S4 to S6), and perform the inversion for a static solution (fig. S3). The final model is then used to estimate the entire surface deformation field and assess residuals (fig. S8 to S11). A model compatible with all the static data is displayed in Fig. 2b. North of the epicenter, the motion on the northeastern side of the surface trace (blue) is larger than that (red) on the southwest. This asymmetry is a clear evidence that faults F2 and F3 are dipping in opposite directions (see figs. S4 to S11 for modeling details).

To determine the time evolution of rupture, we jointly inverted the seismological and geodetic data (remote sensing and GPS). The model is parameterized in terms of the distribution of slip (characterized by rake and amplitude of slip at each node), the rupture velocity and rise time¹⁰.

The static slip distribution corresponding to the model obtained from the joint inversion of the geodetic, remote sensing, and seismological data (Fig. 3b) is very close to the solution obtained from the inversion of the static deformation data (Table 1). The only difference is that slip on F1 cannot be constrained from the geodetic data and is better determined from the seismological data. The total moment of the joint inversion model is $9.9 \times 10^{19} \text{ N} \cdot \text{m}$, which is calculated by summing up the contribution of each sub-fault. The moment tensor is actually very close to the GCMT solution². The double-couple moment is $7.4 \times 10^{19} \text{ N} \cdot \text{m}$ and the CLVD component is $2.1 \times 10^{19} \text{ N} \cdot \text{m}$. This model provides a remarkably good fit to the seismological data (figs. S13 and S14) demonstrating the internal consistency of the whole dataset.

Overall, most of the energy release occurred at depths less than 9 km with slip reaching up to 6 m. The inferred rupture velocity is quite variable and relatively low, about 2.5 km/s on average. The moment release history reflects the successive rupture of different asperities on faults F1 to

F4 (zones with locally high seismic slip) whose location is essentially constrained by the geodetic data (Fig. 3). The earthquake started with a dominantly normal sub-event on F1. This sub-event was not very impulsive and lasted for about 8s, which is a relatively long duration for an M_w 6.3 earthquake. There was a still smaller event a few seconds earlier which can be seen in some teleseismic waveforms (fig. S14). The event on F1 triggered rupture of segments F2 to the north and F3 to the south, F2 produced a sharp pulse of moment release 16s to 21s after the onset of the rupture. The peak in the moment release rate occurred around 27s when the rupture reached nearly simultaneously the high slip patches on F2 and F3. Altogether the rupture lasted about 45-50s.

The distribution of co-seismic slip and aftershocks suggest that the seismogenic zone extends to depths of only about 10km (Fig. 3c). The depth extent is probably limited by the high crustal temperature in this zone of tectonic transition from of spreading centers and transform faults in the Gulf of California to continental faulting along the San Andreas fault system to the North¹³. The distribution of aftershocks is clearly anti-correlated with coseismic slip, especially north of the epicenter where hypocentral depth of aftershocks and the coseismic slip distribution are better constrained (Fig. 3c). Such an anti-correlation has been observed in a number of previous studies¹⁴⁻¹⁷ suggesting that some of the aftershocks release residual strains near the patches of high slip.

The mainshock started as a moderate sub-event and evolved only ~15 s later into a more significant event (Fig. 3d). This rupture behavior challenges the idea that the final size of large earthquakes can be predicted within seconds of the onset of rupture¹⁸. Further the mainshock initiated at a local structural complexity, due an extensional jog at depth (define by F1) between faults F2 and F3. More generally the complex mainshock rupture illustrates how fault bends and

jogs, not necessarily visible from the surficial fault trace geometry, influence the initiation, evolution and termination of earthquake ruptures¹⁹⁻²².

Table 1. Moment tensor solutions of GCMT and this study.

	M _{rr}	M _{tt}	M _{pp}	M _{rt}	M _{rp}	M _{tp}	M _o	M _{DC}	M _{CLVD}	Unit
GCMT	-2.49	-5.94	8.43	0.56	-0.14	-0.86		7.28	2.84	10 ¹⁹ (N·m)
Static inv.	-1.42	-6.42	7.84	0.11	-1.05	-1.55	9.91	7.50	2.11	10 ¹⁹ (N·m)
Joint inv.	-2.03	-6.07	8.10	-0.23	-1.28	-1.62	9.90	7.36	2.14	10 ¹⁹ (N·m)

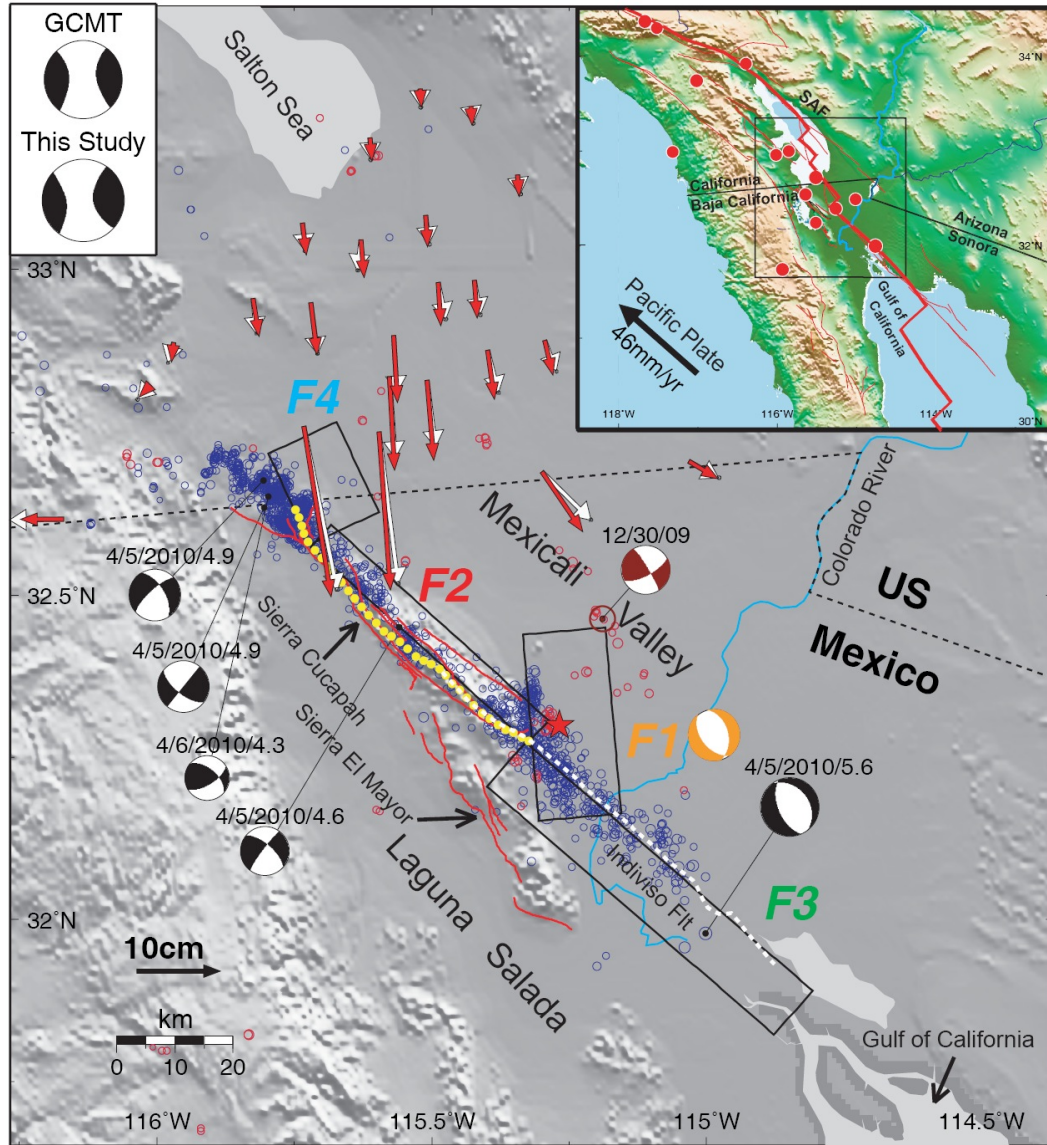


Figure1. Seismotectonic setting of EMC Earthquake and aftershocks. Inset shows historic seismicity with earthquakes ($M > 6.5$, red dots), main active faults (thin red lines) and approximate location of the plate boundary (heavy red line). The black rectangle region is enlarged in which the yellow and white dots denote the fault off-sets determined by SPOT imaging and sub-pixel correlations. Open circles show seismicity ($M > 2.5$) 4 month before (red) and 11 days after (blue) the earthquake, relocated with the Double Difference method²³ and the red lines indicate known surface faults. Moment tensor of GCMT and derived from our study are shown in the left top corner. Mechanisms of 5 large aftershocks are displayed as black beach balls with event dates and magnitudes above. The dark red beach ball and circle

indicates the Dec.30, 2009 Mw5.8 earthquake. The geometry of faults used in the inversion is projected to the free-surface and indicated as F1, F2, F3 and F4. The focal mechanism of the first event, which is obtained by inverting the first 15 seconds of teleseismic P-waves, is displayed in orange. The red star indicates the epicenter of first normal event. Arrows to the north of the US and Mexico border show the horizontal component of the co-seismic displacements measured at the PBO GPS stations (data in white, with 95% confidence ellipses, and synthetic in light red).

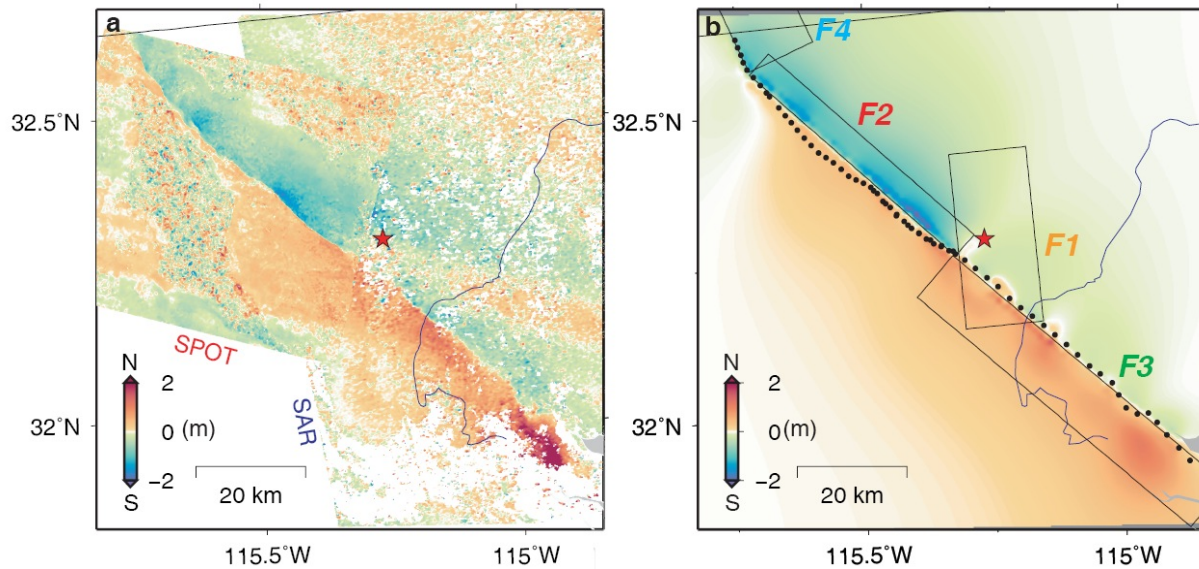


Figure 2. N-S surface displacements measured from sub-pixel correlation of optical and SAR images. (a) Map of near-field co-seismic ground displacement measured from the sub-pixel correlation of SAR amplitude images²⁴ and optical SPOT images^{25,26} acquired before and after the earthquake (see Supplement for details). The SPOT measurements are over-printing the SAR azimuth offsets. **(b)** Prediction from the preferred model. The blue colors indicate motion to the south and red to north, indicating right-lateral slip on the fault. The red star shows location of the epicenter where the rupture sequence initiated. The black dots displays the fault trace as determined from the SAR and optical images correlation. Thin black rectangles show surface projection of the idealized fault segments used in the modeling.

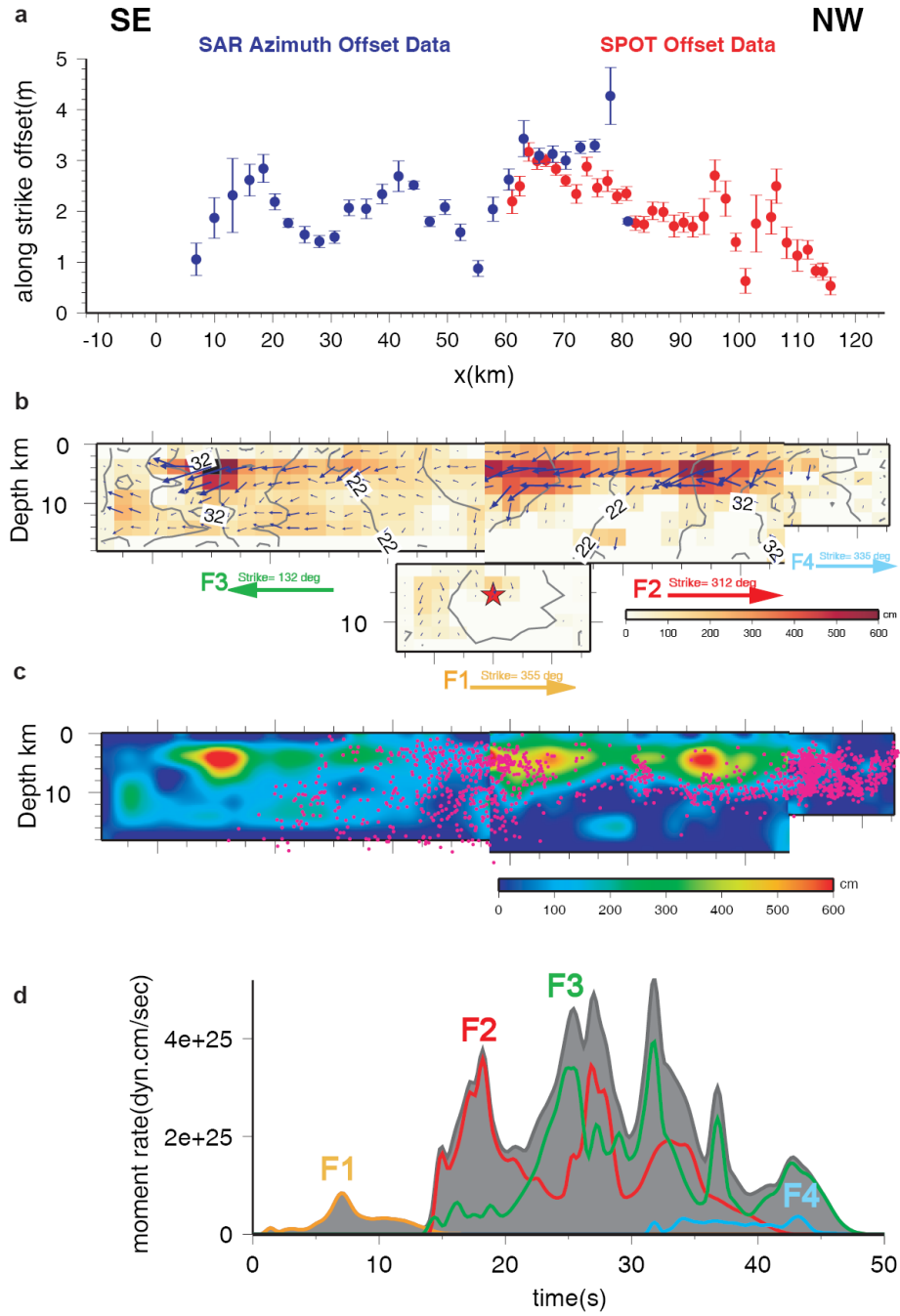


Figure 3. Slip distribution offsets and rupture history. (a) Surface displacements derived from serial profiles across the fault trace using the horizontal displacement field measured from the correlation of SAR (blue) and SPOT (red) images. (b) Cumulative slip distribution (arrows show slip vectors, and color

coding shows amplitude of slip) and isochrons of the seismic rupture. The rupture times are given relative to the onset of slip at the epicenter on F1. Note the large displacements around 17s and 27s on F2. (c) Comparison of relocated aftershocks projected on the faults with co-seismic slip distribution (smoothed). (d) Source time function showing the time evolution of moment rate released during the whole rupture sequence. The contribution of each fault segment is indicated by a different color with the same color code as in panel (b).

Reference

- 1 Sieh, K. *et al.* Near-Field Investigations of the Landers Earthquake Sequence, April to July 1992. *Science* **260**, 171-176 (1993).
- 2 Harvard CMT solutions can be accessed at <http://www.globalcmt.org/CMTsearch.html>.
- 3 Atwater, T. & Stock, J. Pacific North America plate tectonics of the Neogene southwestern United States: An update. *Int. Geol. Rev.* **40**, 375-402 (1998).
- 4 Fletcher, J. M. & Spelz, R. M. Patterns of Quaternary deformation and rupture propagation associated with an active low-angle normal fault, Laguna Salada, Mexico: Evidence of a rolling hinge? *Geosphere* **5**, 385-407 (2009).
- 5 Gonzalez-Garcia, J. J. *et al.* Seismotectonics of the 2010 El Mayor Cucapah - Indiviso Earthquake and its Relation to Seismic Hazard in Southern California. *AGU Fall Meeting*, T53B-2117 (2010).
- 6 Hartzell, S. & Helmberger, D. V. Strong-Motion Modeling of the Imperial-Valley Earthquake of 1979. *Bull. Seismol. Soc. Am.* **72**, 571-596 (1982).
- 7 Ji, C., Helmberger, D. V., Song, T.-R. A., Ma, K.-F. & Wald, D. J. Slip distribution and tectonic implications of the 1999 Chi-Chi, Taiwan earthquake. *Geophys. Res. Lett.* **28**, 4379-4382 (2001).
- 8 Delouis, B., Giardini, D., Lundgren, P. & Salichon, J. Joint inversion of InSAR, GPS, teleseismic, and strong-motion data for the spatial and temporal distribution of earthquake slip: Application to the 1999 Izmit mainshock. *Bull. Seismol. Soc. Am.* **92**, 278-299 (2002).
- 9 Wesnousky, S. G. Predicting the endpoints of earthquake ruptures. *Nature* **444**, 358-360 (2006).
- 10 Ji, C., Wald, D. & Helmberger, D. V. Source Description of the 1999 Hector Mine, California Earthquake, Part I: Wavelet Domain Inversion Theory and Resolution Analysis. *Bull. Seismol. Soc. Am.* **92**, 1192-1207 (2002).
- 11 Avouac, J. P., Ayoub, F., Leprince, S., Konca, O. & Helmberger, D. V. The 2005, M-w 7.6 Kashmir earthquake: Sub-pixel correlation of ASTER images and seismic waveforms analysis. *Earth Planet. Sci. Lett.* **249**, 514-528 (2006).
- 12 Lohman, R. B. & Simons, M. Some thoughts on the use of InSAR data to constrain models of surface deformation: Noise structure and data downsampling. *Geochemistry Geophysics Geosystems* **6**, - (2005).
- 13 Blanpied, M. L., Lockner, D. A. & Byerlee, J. D. Frictional Slip of Granite at Hydrothermal Conditions. *J. Geophys. Res.* **100**, 13045-13064 (1995).
- 14 Yagi, Y., Kikuchi, M. & Sagiya, T. Co-seismic slip, post-seismic slip and aftershocks associated with two large earthquakes in 1996 in Hyugia-nada, Japan. *Earth Planet. Space* **53**, 793-803 (2001).

- 15 Hsu, Y. J. *et al.* Frictional afterslip following the 2005 Nias-Simeulue earthquake, Sumatra. *Science* **312**, 1921-1926 (2006).
- 16 Sladen, A. *et al.* Source model of the 2007 M-w 8.0 Pisco, Peru earthquake: Implications for seismogenic behavior of subduction megathrusts. *J. Geophys. Res.* **115**, - (2010).
- 17 Tilmann, F. J. *et al.* The updip seismic/aseismic transition of the Sumatra megathrust illuminated by aftershocks of the 2004 Aceh-Andaman and 2005 Nias events. *Geophys. J. Int.* **181**, 1261-1274 (2010).
- 18 Ellsworth, W. L. & Beroza, G. C. Seismic Evidence for an Earthquake Nucleation Phase. *Science* **268**, 851-855 (1995).
- 19 King, G. C. & Nabelek, J. The role of fault bends in faults in the initiation and termination of earthquake rupture. *Science* **283**, 984-987 (1985).
- 20 Wesnousky, S. G. Displacement and geometrical characteristics of earthquake surface ruptures: Issues and implications for seismic-hazard analysis and the process of earthquake rupture. *Bull. Seismol. Soc. Am.* **98**, 1609-1632 (2008).
- 21 Harris, R., Archuleta, R. & Day, S. Fault steps and the dynamic rupture process: 2-D numerical simulations of a spontaneously propagating shear fracture. *Geophys. Res. Lett.* **18**, 893-896 (1991).
- 22 Bouchon, M., Campillo, M. & Cotton, F. Stress field associated with the rupture of the 1992 Landers, California, earthquake and its implications concerning the fault strength at the onset of the earthquake. *J. Geophys. Res.* **103**, 21091-21097 (1998).
- 23 Hauksson, E. *et al.* The 2010 Mw 7.2 El Mayor-Cucapah Earthquake Sequence, Baja California, Mexico and Southernmost California, USA: Active Seismotectonics along the Mexican Pacific Margin. *Pure Appl Geophys*, doi:DOI: 10.1007/s00024-010-0209-7 (2010).
- 24 Michel, R., Avouac, J. P. & Taboury, J. Measuring near field coseismic displacements from SAR images: application to the Landers earthquake. *Geophys. Res. Lett.* **26**, 3017-3020 (1999).
- 25 Van Puymbroeck, N., Michel, R., Binet, R., Avouac, J. P. & Taboury, J. Measuring earthquakes from optical satellite images. *Appl. Opt.* **39**, 3486-3494 (2000).
- 26 Leprince, S., Barbot, S., Ayoub, F. & Avouac, J. P. Automatic and precise orthorectification, coregistration, and subpixel correlation of satellite images, application to ground deformation measurements. *Ieee Transactions on Geoscience and Remote Sensing* **45**, 1529-1558, doi:10.1109/tgrs.2006.888937 (2007).

Acknowledgement

This work was funded by NSF, USGS, the Gordon and Betty Moore Foundation, NASA, and SCEC. Regional seismic data provided by SCSN and RESNOM. The Incorporated Research Institutions for Seismology (IRIS) Data Management System (DMS) was used to access the Global Seismographic Network data. The GPS analyses were obtained from the Earthscope Plate Boundary Observatory (PBO) data products system and UNAVCO. Optical data provided by USGS. Envisat data is copyright 2009, 2010 ESA and was obtained from the WInSAR archive and the Group on Earth Observation Geohazards Supersite virtual archive. ALOS data is copyright METI, JAXA and was obtained from the Alaska Satellite Facility Level 1 Data Pool. Part of this research was performed at the Jet Propulsion Laboratory, California Institute of Technology under contract with the National Aeronautics and Space Administration. We thank CICESE colleagues Javier Gonzalez and John Fletcher for their support and interest. This is Tectonics Observatory contribution #.